Article

Direct magnetic imaging of fractional Chern insulators in twisted $MoTe_2$

https://doi.org/10.1038/s41586-024-08153-x

Received: 15 May 2024

Accepted: 4 October 2024

Published online: 20 November 2024

Check for updates

Evgeny Redekop[1], Canxun Zhang[1], Heonjoon Park[2], Jiaqi Cai[2], Eric Anderson[2], Owen Sheekey[1], Trevor Arp[1], Grigory Babikyan[1], Samuel Salters[1], Kenji Watanabe[3], Takashi Taniguchi[4], Martin E. Huber[5], Xiaodong Xu[2,6] & Andrea F. Young[1]✉

Orbital magnetization provides a sensitive probe of topology and interactions, with particularly rich phenomenology in Chern insulators in which the topological edge states carry large equilibrium currents. Here we use a nanoscale superconducting sensor[1,2] to map the magnetic fringe fields in twisted bilayers of $MoTe_2$, in which transport[3,4] and optical sensing[5,6] experiments have revealed the formation of fractional Chern insulator (FCI) states at zero magnetic field. We observe oscillations in the local magnetic field associated with fillings $\nu = -1, -2/3, -3/5, -4/7$ and $-5/9$ of the first moiré hole band, consistent with the formation of FCIs at these fillings. We determine the local thermodynamic gaps of the most robust FCI state at $\nu = -2/3$, finding $^{-2/3}\Delta$ as large as 7 meV. We also characterize sample spatial disorder, which is dominated by both inhomogeneity in the effective unit cell area[7] as well as inhomogeneity in the band edge offset and bound dipole moment. Our results highlight both the challenges posed by structural disorder in the study of twisted homobilayer moiré systems and the opportunities afforded by the robust nature of the underlying correlated topological states.

Fractional Chern insulators (FCIs) are generalizations of the fractional quantum Hall states to lattice systems with broken time-reversal symmetry. Interest in FCIs arises from the fact that they may emerge as the ground state of interacting fermions on a lattice, including at zero magnetic field for which time-reversal symmetry is broken spontaneously.

FCIs were first observed experimentally in moiré heterostructures composed of graphene and hexagonal boron nitride (hBN) at partial fillings of topological Harper–Hofstadter bands[8] at 30 T magnetic fields. In this context, the applied magnetic field plays a key part in forming the bands leading to energy gaps comparable to those observed in conventional fractional quantum Hall states. Prospects for realizing more robust lattice-based Chern insulators improved with the realization of narrow, topologically nontrivial bands at zero magnetic field in moiré systems, including twisted bilayer graphene[9], rhombohedral graphene multilayers aligned to hBN[10] and transition metal dichalcogenide bilayers[11–15]. In these systems, experiments showed evidence of time-reversal symmetry breaking by spontaneous valley polarization, manifesting most dramatically with the observation of quantized integer anomalous Hall effects at zero magnetic field[16–20], as well as FCI states at finite applied magnetic fields[21].

Most recently, zero-magnetic-field FCIs were discovered in rotationally faulted bilayers of $MoTe_2$ near 4° angle[3–6,22] and in rhombohedral graphene pentalayers aligned to an hBN substrate[23]. These observations raise key questions about the microscopic origin of these states, their competition with other correlated ground states and the possibility of realizing new topological phases absent in partially filled Landau levels, leading to a growing body of theoretical work[24–34].

Local magnetometry of FCIs

In a Chern insulator, equilibrium currents carried by the chiral edge states contribute a topological magnetization

$$\Delta m = \frac{C\Delta}{\Phi_0}, \tag{1}$$

which represents the change in magnetization across the incompressible bulk gap (here C is the total Chern number, Δ is the thermodynamic energy gap and Φ_0 is the non-superconducting flux quantum). This universal contribution occurs atop a non-universal background of spin and orbital magnetic moments arising from the filled electronic states in the sample bulk. Here we take advantage of the compatibility of zero-magnetic-field FCIs with superconducting sensors to perform ultrasensitive magnetometry of the fringe magnetic fields associated with spin and orbital magnetism in twisted $MoTe_2$ on the submicron scale.

We use an indium nSOT sensor with an effective diameter of approximately 200 nm to map the fringe magnetic field above several twisted bilayer $MoTe_2$ samples with a spatial resolution of about 250 nm. Our sensors represent a notable improvement over the state-of-the-art sensors[35], with a measured sensitivity of 0.2 nT $Hz^{-1/2}$ (Methods and Extended Data Fig. 1) corresponding to $4n\Phi$ $Hz^{-1/2}$, where Φ_0 is the superconducting flux quantum. Our samples consist of a twisted bilayer $MoTe_2$ active layer encapsulated by hBN dielectrics with graphite top and bottom gates (Fig. 1a and Extended Data Fig. 2). Together, the gates

[1]Department of Physics, University of California Santa Barbara, Santa Barbara, CA, USA. [2]Department of Physics, University of Washington, Seattle, WA, USA. [3]Research Center for Electronic and Optical Materials, National Institute for Materials Science, Tsukuba, Japan. [4]Research Center for Materials Nanoarchitectonics, National Institute for Materials Science, Tsukuba, Japan. [5]Departments of Physics and Electrical Engineering, University of Colorado Denver, Denver, CO, USA. [6]Department of Materials Science and Engineering, University of Washington, Seattle, WA, USA. ✉e-mail: andrea@physics.ucsb.edu

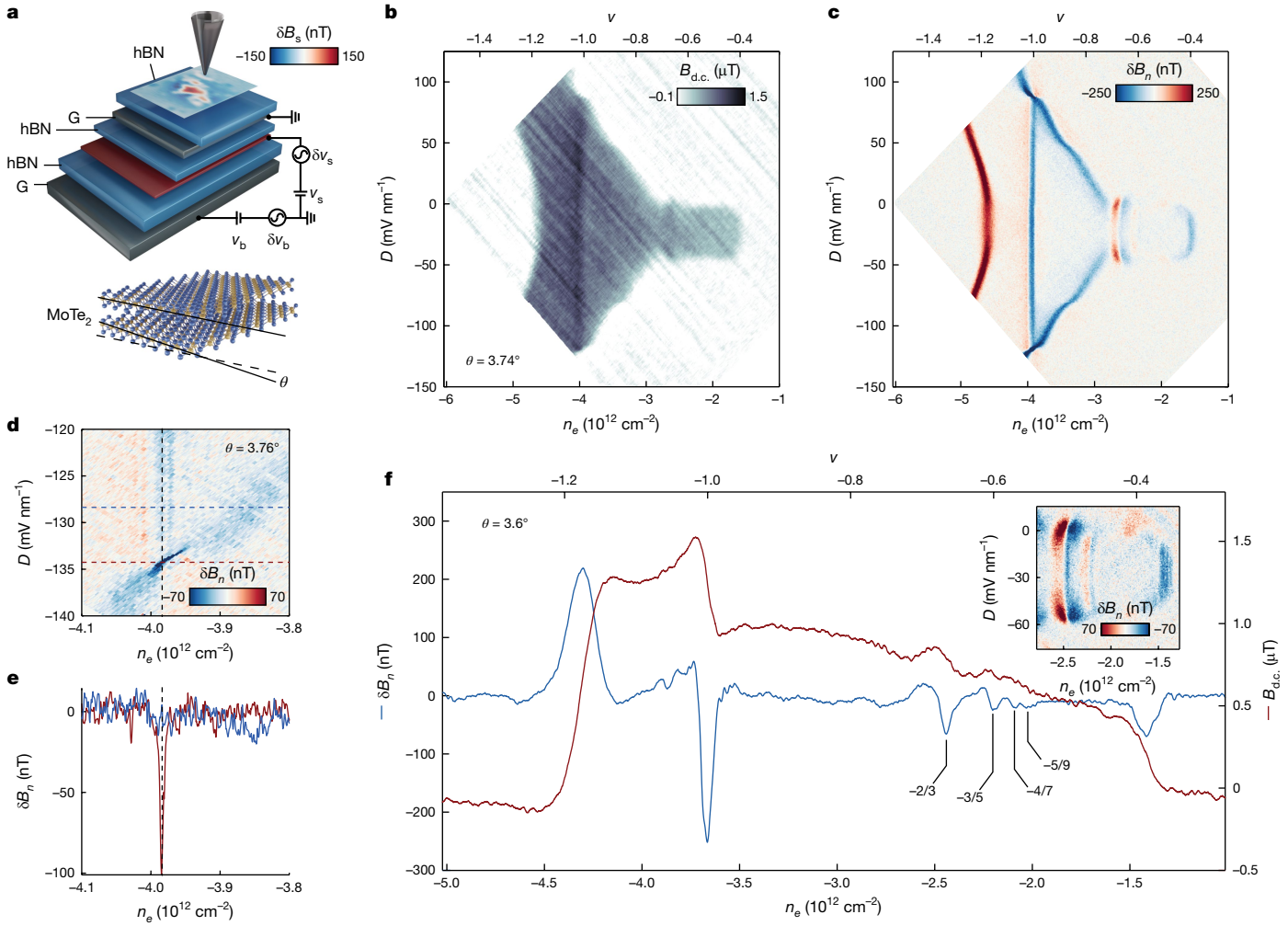

Fig. 1 | Local magnetometry of FCIs in twisted $MoTe_2$. **a**, Schematic of the experimental geometry, showing an nSOT sensor above a van der Waals heterostructure consisting of a dual graphite-gated twisted $MoTe_2$ bilayer with a twist angle of 3.7°. Static voltages v_s and v_b and modulated voltages δv_s and δv_b are applied to the sample and bottom gate as shown, allowing finite-frequency readout of the modulated magnetization, shown in overlay for finite δv_s and $\delta v_b = 0$ at moiré filling $\nu = -1$ in sample B. **b**, Static magnetic field $B_{d.c.}$ measured at a single point as a function of charge carrier density n_e and applied electric displacement field D at 1.6 K in sample A. **c**, δB_n with an applied modulation of $\delta n \approx 3.8 \times 10^{10}$ cm^{-2}, measured at the same position as the data in **b**. **d**, δB_n measured with $\delta n \approx 3.8 \times 10^{9}$ cm^{-2} near the valley polarization transition at $\nu = -1$. The sharp signal is indicative of a first-order phase transition at which the magnetization vanishes. **e**, Two traces extracted from **d**. **f**, δB_n and $B_{d.c.}$ measured at $T = 1.6$ K, $B = 34$ mT and $D = -29$ mV nm^{-1}; for δB_n the applied $\delta n \approx 3 \times 10^{10}$ cm^{-2}. We identify the peak at $\nu \approx -1.175$ and dip at $\nu \approx -0.39$ with the boundaries of the magnetic phase, and the five minima at $\nu = -1$, $-2/3$, $-3/5$, $-4/7$ and $-5/9$ with the edge state magnetization of Chern insulator states. Inset, δB_n measured with an applied modulation $\delta n \approx 1.9 \times 10^{10}$ cm^{-2} in the FCI regime, showing D-independent minima at $\nu = -2/3$ and $-3/5$ within the valley-polarized regime.

allow independent control of the charge carrier density n_e and electric displacement field D. The graphite gates are transparent to the fringe magnetic fields, making magnetic imaging an ideal tool for probing the n_e and D-tuned phase diagram. We measure the fringe fields either in direct current mode by the static magnetic field $B_{d.c.}$ at fixed n and D or in alternating current mode through lock-in readout of the magnetic response to modulations applied to the sample and/or top and bottom gate voltages. Appropriate choice of the relative magnitude and phase of these voltages allows us to measure either the density or displacement field derivatives of the fringe field, $\delta B_n \approx \frac{\partial B_{d.c.}}{\partial n_e}\delta n_e$ and $\delta B_D \approx \frac{\partial B_{d.c.}}{\partial D}\delta D$.

Figure 1b shows $B_{d.c.}$ measured locally at a height 50 nm above the surface of sample A. Magnetic signal is observed in a broad region of the phase diagram centred at a low displacement field, consistent with previous optical and transport measurements[3,6,20]. We associate this regime with a valley-imbalanced ferromagnetic phase. Features previously identified as Chern insulators at $\nu = -1$ and $\nu = -2/3$ are visible in this image as subtle vertical lines. These become visible in measurements of δB_n, shown in Fig. 1c. In this contrast mode, the decrease in magnetization with increasing chemical potential, characteristic of the edge states of Chern insulators with negative C, manifests as a sharp, negative (blue) signal that appears at a D-independent density. Similar phase diagrams were obtained from three samples, as shown in Extended Data Fig. 2. The charge carrier density in the $tMoTe_2$ may be independently calibrated using magnetic features associated with Landau levels in the graphite top gate, and measurements in device C confirm that the negative δB_n feature associated with the $\nu = -2/3$ state occurs at filling factor of $\nu = 0.66 \pm 0.02$ (Extended Data Fig. 3). Previous measurements of the same device[3] have shown quantized Hall resistance and magnetic-field-dependent density consistent with Chern insulator states at $\nu = -1$, $-2/3$ and $-3/5$ with Chern number $C = \nu$.

Our high-sensitivity local measurement allows us to examine several aspects of the phase diagram that have been ambiguous in previous studies of the same system. For example, we find that although the signal associated with the Chern insulator gap is the strongest at zero effective displacement field (Extended Data Fig. 4), it remains finite

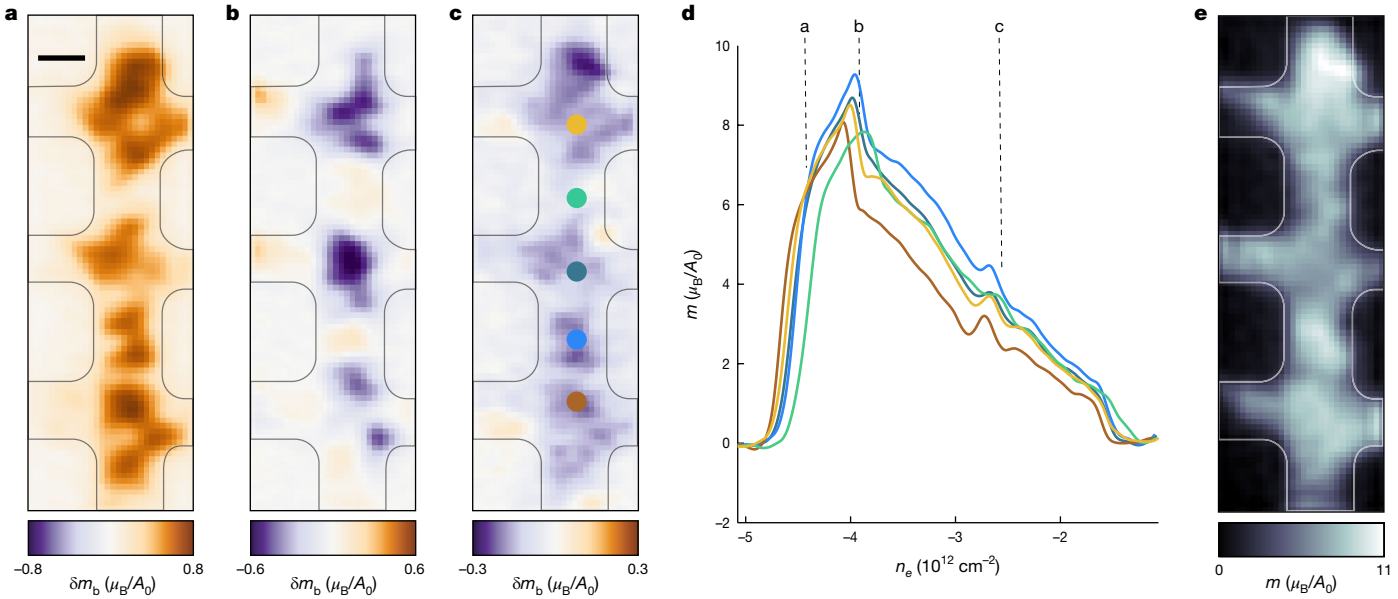

Fig. 2 | Reconstructing local magnetization. a–**c**, Differential magnetization δm_b reconstructed from spatial maps of $\delta B_b \approx (\partial B/\partial v_b)\delta v_b$, with δv_b corresponding to $\delta n = 2.1 \times 10^{10}$ cm^2 measured at $D = -29$ mV nm^{-1} and density corresponding to $\nu \approx -1.2$ (**a**), $\nu \approx -1$ (**b**) and $\nu \approx -0.66$ (**c**). Here $A_0 = 25.9$ nm^2 is the superlattice unit cell area corresponding to a twist angle of 3.7°. **d**, Total out-of-plane magnetization m, calculated by integrating the differential magnetization for the spatial positions indicated in **c**. **e**, Spatial image of m at $D = -29$ mV nm^{-1} and $\nu \approx -1.1$. Scale bar, 500 nm.

until the sharp, D-tuned phase transitions to a non-magnetic phase. This is confirmed by low-excitation, high-resolution measurements of δB_n in the vicinity of the phase transition at large negative D shown in Fig. 1d, in which an exceptionally sharp feature associated with a decrease in magnetization appears at $\nu = -1$. As shown in Fig. 1e, the fringe magnetic field associated with this feature is about one order of magnitude larger than those associated with the Chern insulator edge states at $\nu = -1$, and the large negative signal occurs over a narrow range of D and n_e. This is expected for a first-order phase transition between a valley-imbalanced Chern insulator and a topologically trivial insulator with no net magnetization (see additional data in Extended Data Fig. 5). We conclude that the first-order phase transition in valley polarization occurs before any displacement field-tuned change in band topology, and find no evidence for a valley-imbalanced metallic state. Notably, although the valley-imbalanced transition is sharp at $\nu = -1$, in which the transition occurs between a Chern insulator and a topologically trivial correlated insulator[3], it is broad in the metallic regimes between commensurate filling factors.

Figure 1f shows a high-resolution trace of both $B_{d.c.}$ and δB_n acquired at $T = 1.6$ K, $B = 34$ mT and $D = -29$ mV nm^{-1}. In this dataset, we observe oscillations in the local magnetic field, with oscillation minima associated with band fillings $\nu = -1, -2/3, -3/5, -4/7$ and $-5/9$. High-resolution data acquired near filling $\nu = -1/2$ as a function of both n_e and D (Fig. 1f, inset) shows negative δB_n features at $\nu = -2/3$ and $\nu = -3/5$, which (mimicking the behaviour at $\nu = -1$) persist to the valley polarization transition. We associate the negative features with the FCI gaps. However, they are accompanied by a positive δB_n feature at slightly higher hole density. We associate this feature with a non-topological magnetization that arises for small doping of the system away from the FCI gaps.

Current theoretical understanding of twisted bilayer $MoTe_2$ suggests that the single-particle wave functions of the lowest energy moiré hole band in a single valley resemble those of the lowest energy Landau level in a two-dimensional electron system, with an emergent composite Fermi liquid state at half filling[34,36]. As in fractional quantum Hall systems in partially filled Landau levels, then, a sequence of incompressible states are observed at fillings $p/(2p \pm 1)$ corresponding to the quantum oscillations of the composite fermions in the effective magnetic field[37], which in this case is a completely interaction induced property of the magnetic ground state. In this picture, the oscillations we observe in Fig. 1f represent de Haas–van Alphen oscillations in the magnetization of the composite fermions in the density-tuned emergent magnetic field. Our observation of oscillations in the magnetization, $m = \mathrm{d}F/\mathrm{d}B$, where F is the free energy of the system, can be taken as direct evidence for the emergence of topological gaps whose charge density is magnetic field dependent.

Quantifying local magnetization

The data in Fig. 1 provide a qualitative picture of the microscopic phase diagram. To quantitatively measure the magnetization, we take spatial scans of $B_{d.c.}$ and δB_b and use an inversion algorithm to reconstruct the static magnetization m and differential magnetization change in response to a change in bottom gate voltage, $\delta m_b = \partial m/\partial v_b \times \delta v_b$ (Methods and Extended Data Fig. 6). This analysis assumes that magnetic moments point only in the out-of-plane direction, an assumption that is well justified in strongly spin–orbit-coupled twisted $MoTe_2$. Figure 2a–c shows δm_b images acquired at applied $D = -29$ mV nm^{-1} and n_e corresponding to $\nu \approx -1.2$, $\nu \approx -1$ and $\nu \approx -2/3$, respectively. The sample magnetization is inhomogeneous on submicron scales, a feature universal to all samples measured. Figure 2d shows the n_e-dependent total m, obtained by integrating δm_b, at several different points in the device shown in Fig. 2c. The static magnetization m scales approximately linearly with n_e, consistent with a large, non-topological orbital magnetization in the ferromagnetic phase ranging from 6 to 8 μ_B per hole, where μ_B is the Bohr magneton. This agrees with estimates for the renormalization of the spin moment arising from atomic scale spin–orbit coupling determined from band theory and optical experiments[38–40]. Despite the strong spatial inhomogeneity in the internal structure of the ferromagnetic region, the entire sample is magnetized, consistent with valley polarization being a robust feature of the phase diagram across a range of sample parameters (Fig. 2e).

Our quantitative reconstruction of the magnetization may also be used to directly determine the Chern insulator gaps using equation (1).

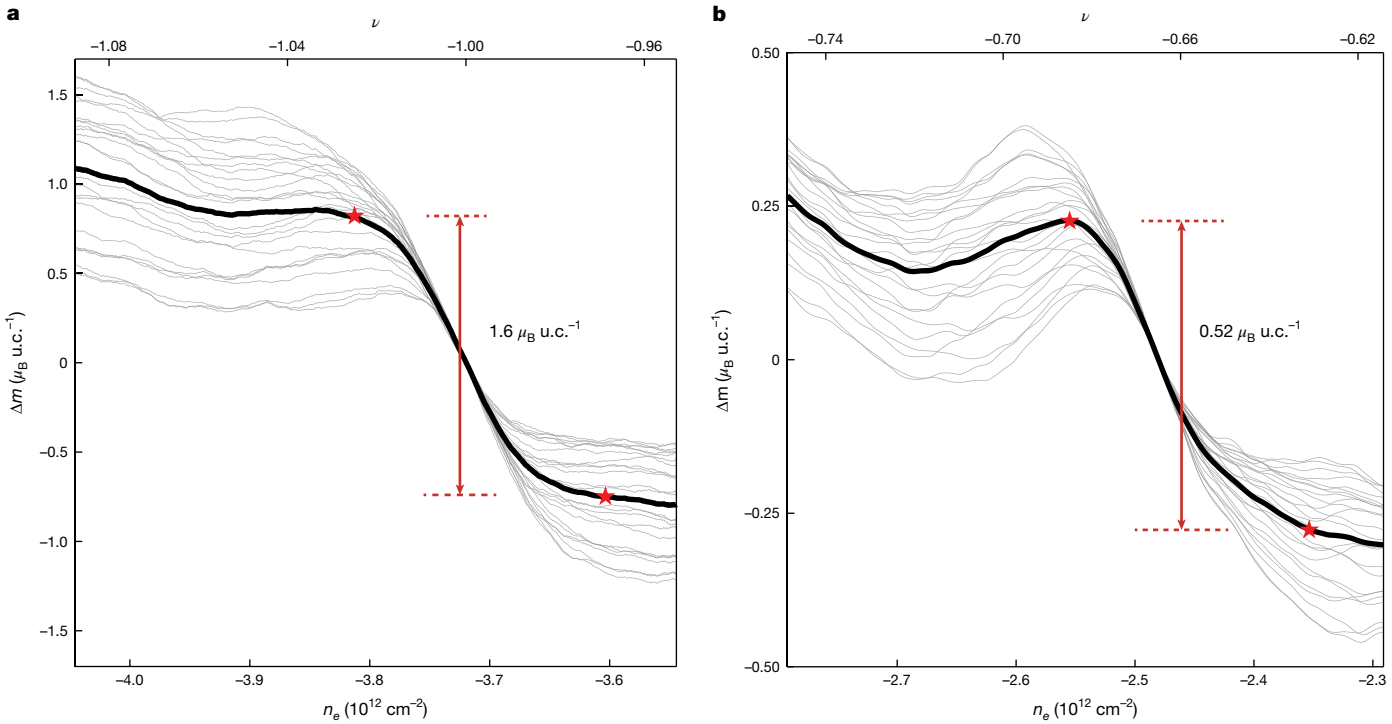

Fig. 3 | Thermodynamic gaps. a, Magnetization change Δm (referenced to the centre of the local $\nu = -1$ gap) in a region in which the local twist angle $\theta \approx 3.64°$. Grey curves correspond to different spatial positions within a 300×300 nm^2 region (Extended Data Fig. 8). The black curve is the average. We find a change of $\Delta m_{-1} = 1.6(1)\,\mu_B$ u.c.$^{-1}$ across $\nu = -1$ gap, corresponding to $^{-1}\Delta = 14(1)$ meV gap for $C = -1$. **b**, Δm for $\nu = -2/3$ (referenced to the centre of the $\nu = -2/3$ gap), measured at the same points as in **a**. $\Delta m_{-2/3} = 0.52(4)\,\mu_B$ u.c.$^{-1}$, corresponding to the thermodynamic gap $^{-2/3}\Delta = 7.0(5)$ meV, assuming $C = -2/3$.

Figure 3a,b shows m in the vicinity of $\nu = -1$ and $\nu = -2/3$, measured with higher resolution in n_e and real space as compared with the data in Fig. 2d. We extract the change in magnetization from the extent of the negative-slope regions at each rational filling factor, obtaining $\Delta m_{-1} = 1.6(1)\,\mu_B$ u.c.$^{-1}$ and $\Delta m_{-2/3} = 0.52(4)\,\mu_B$ u.c.$^{-1}$, where u.c. is the unit cell area of moiré lattice. Assuming $C = \nu$ (consistent with transport measurements of the same sample[3]), this yields thermodynamic energy gaps of $^{-1}\Delta = 14(1)$ meV and $^{-2/3}\Delta = 7.0(5)$ meV. Similar results were also obtained from a second device (Extended Data Fig. 7).

The ranges in the measured gap sizes reflect the standard deviation in gap values measured values within a small area of the device (Extended Data Fig. 8) rather than experimental uncertainty. Our determination of the gap sizes is, however, susceptible to several sources of error (Methods).

In a clean quantum Hall system, the thermodynamic gap measures the energy to add one electron of charge to the gapped ground state. In states in which the excitations carry only an integer charge, this is equivalent to the thermal activation gap. In states in which elementary excitations carry fractional charge $e^* = e/q$. However, the thermal activation gap measured in transport is expected to be smaller than the thermodynamic gap by a factor of q. In a disorder-free, partially filled Landau level with Coulomb interactions, the ratio of the thermodynamic gaps at $\nu = 1$ and $\nu = 1/3$ is expected to be approximately 4 (ref. 41); we find a ratio of approximately 2—that is, the fractional state is larger in comparison with the integer state than for a Landau level system. Our data also show a notable discrepancy when compared with transport measurements. From our measurements, $^{-1}\Delta$ corresponds to a thermal activation gap of 150 K, approximately five times larger than the 30 K found in transport measurements[3]. However, our measurement of $^{-2/3}\Delta \approx 7$ meV corresponds to an estimated thermal activation gap of approximately 27 K, roughly consistent with transport measurements[3]. Quantitatively reconciling these observations requires a detailed theory that accounts for both the band effects unique to lattice Chern bands and the contrasting effects of disorder on the thermodynamic and transport gaps at integer and fractional filling.

As a final point of comparison, the energy scales measured here are also similar in scale to thermodynamic gaps measured in monolayer graphene fractional quantum Hall systems at $B \approx 14$ T in a similar electrostatic geometry[42]. We note, however, that sample inhomogeneity on length scales smaller than that of our local probe may well contribute to the lowering of the measured thermodynamic gaps in twisted $MoTe_2$ relative to the intrinsic gap size. The intrinsic gaps may thus be even larger than reported here, consistent with theoretical analyses that find $MoTe_2$ bilayers to be equivalent to conventional quantum Hall states at magnetic fields as large as 160 T (ref. 36).

Sources of disorder in twisted $MoTe_2$

A key consideration in the interpretation of both transport and bulk thermodynamic data in moiré systems is sample disorder. In particular, variations in structural parameters can make the same Chern insulator state occur at different values of the applied gate voltages in different parts of the sample; the sample will then not be uniformly gapped and measurements will be strongly dependent on the size and shape of the probed region. Macroscopic thermodynamic probes average both incompressible and compressible regions, reducing the measured thermodynamic gap, whereas transport measurements may see edge state transport shorted by bulk conducting regions of the sample. The effect of structural disorder is shown in Fig. 4a, which shows δm_b as a function of the sum of the applied gate voltages to the top and bottom gates, $V \equiv v_t + v_b$ (with D held constant) and the spatial coordinate along a trajectory that runs along the spine of the Hall bar sample. The applied gate voltage required to reach the same moiré density varies by about 10%. As the Chern insulator states at $\nu = -1$ and $\nu = -2/3$ occur at fixed, known filling of the moiré superlattice, the voltages at

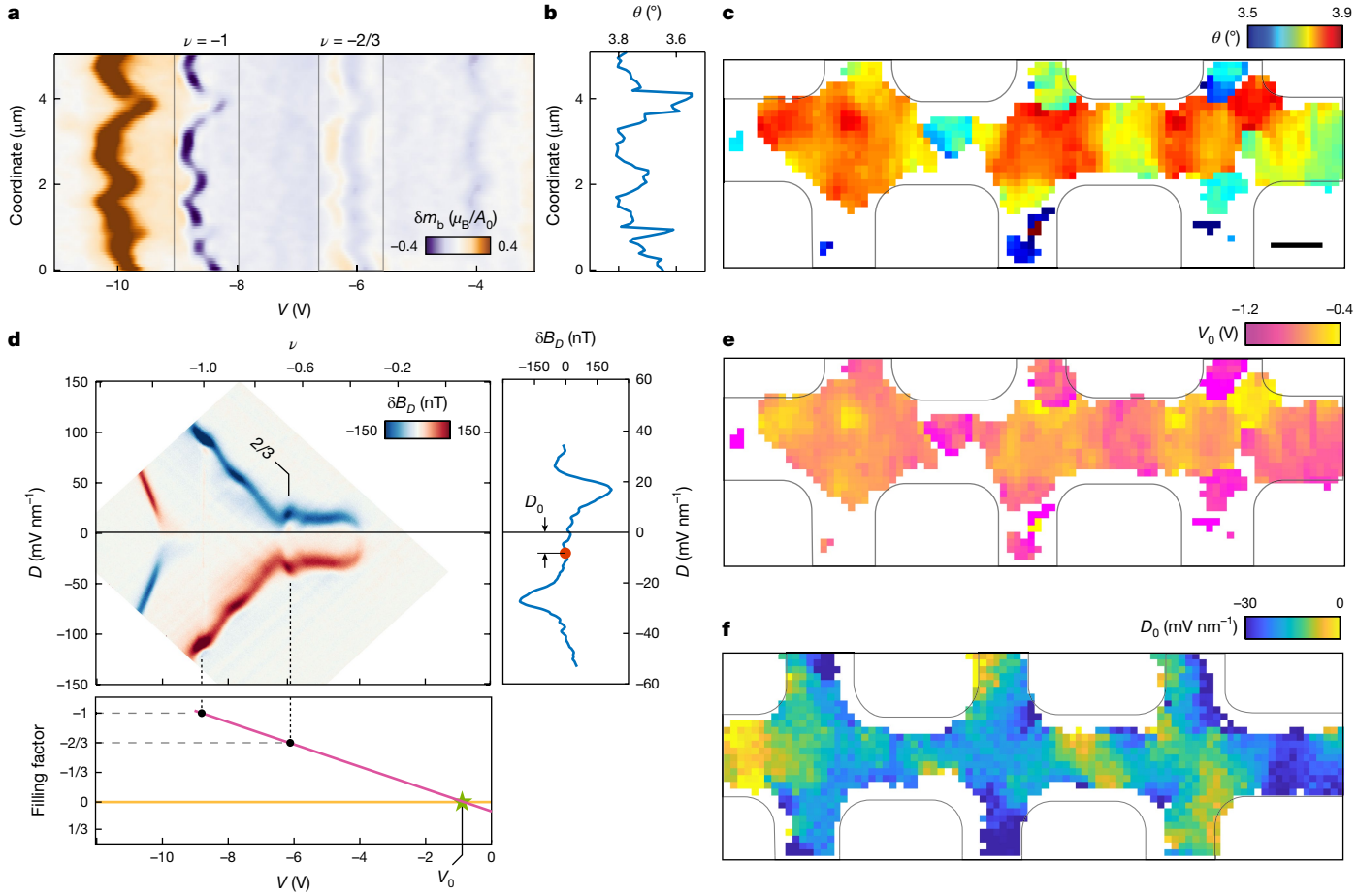

Fig. 4 | Sources of disorder. a, δm_b as a function of $V \equiv \upsilon_t + \upsilon_b$ along a trajectory running along the centre of the device with $\delta\upsilon_b = 20$ mV. Features near $V = -9$ V and −6 V correspond to topological gaps at $\nu = -1$ and $\nu = -2/3$, respectively. **b**, Effective interlayer twist angle along the spatial trajectory of **a**, extracted from the density difference between $\nu = -1$ and $\nu = -2/3$ magnetization features. **c**, Local twist angle map in device A. **d**, δB_D as a function of V and D with $\delta D \approx 4$ mV nm^{-1}. Apart from the twist angle, the voltages corresponding to Chern insulators at $\nu = -1$ and $\nu = -2/3$ are used to extract the valence band offset, V_0, corresponding to $n_e = 0$. The D-induced valley-polarization transitions, meanwhile, are used to extract the displacement field offset D_0. **e**, Spatial map of V_0 in device A. **f**, Spatial map of D_0 in device A.

which they appear allow us to extract the moiré density, defined as $n_M^{-1} = \frac{\sqrt{3}a^2}{2\sin\theta}$ using the relation $c(V_{-1} - V_{-2/3}) = n_M/3$, where c is the capacitance per unit area of the two gates. The effective interlayer twist angle θ corresponding to the trajectory in Fig. 4a is plotted in Fig. 4b, whereas a map of the effective twist angle throughout the device is shown in Fig. 4c. Qualitatively, the twist angle map is reminiscent of twisted bilayer graphene[7] with regions of approximately uniform twist angle separated by domain walls in which the effective twist angle changes suddenly.

We also identify additional microscopic sources of disorder. Figure 4d shows measurements of δB_D as a function of D and V. Apart from the twist angle, V_{-1} and $V_{-2/3}$ also allow us to determine the threshold voltage associated with the valence band edge, $V_0 = 3V_{-2/3} - 2V_{-1}$. This quantity, which we term the band edge offset, may be determined by the band gap of the $MoTe_2$ layers as well as bound electric charges (for example, in an impurity band) that must be filled before the first itinerant hole populates the $MoTe_2$ valence band. Figure 4e shows a spatial map of this quantity, which varies by as much as 1 V across the sample. Variations in this parameter are confirmed by chemical potential sensing measurements that leverage the magnetic response of the top graphite gate (see Extended Data Fig. 3). We also find evidence for a built-in dipole moment. As shown in Fig. 4d, the ferromagnetic region of the phase diagram is symmetric about a fixed but non-zero value of D. We associate this displacement field offset D_0 with a built-in electric field, which we find varies spatially on the micron scale as shown in Fig. 4f. This electric field may be associated with heterostrain in the $MoTe_2$ bilayer, which breaks the layer-inversion symmetry of the idealized bilayer system at $D = 0$ mV nm^{-1} and induces bound dipole charge within the layers. Apart from these sources of inhomogeneity, FCI states are observed over most of the sample area, suggesting a certain degree of robustness of the underlying phenomena.

Conclusion

In conclusion, our results highlight both the promise and challenges of twisted homobilayer moiré materials for the study of FCI physics. Although the domain of stability of Chern insulator physics in $tMoTe_2$ is larger than in twisted bilayer graphene[17,43], the samples studied here, nevertheless, show a large range in the effective filling factor at fixed gate voltage. Interferometric detection of quasiparticle statistics[44], for example, typically requires highly uniform two-dimensional electron systems in which the trajectory of the current-carrying edge states can be precisely controlled, requiring marked improvements in sample homogeneity.

Online content

Any methods, additional references, Nature Portfolio reporting summaries, source data, extended data, supplementary information, acknowledgements, peer review information; details of author contributions

and competing interests; and statements of data and code availability are available at https://doi.org/10.1038/s41586-024-08153-x.

1. Finkler, A. et al. Self-aligned nanoscale SQUID on a tip. *Nano Lett.* **10**, 1046–1049 (2010).
2. Vasyukov, D. et al. A scanning superconducting quantum interference device with single electron spin sensitivity. *Nat. Nanotechnol.* **8**, 639–644 (2013).
3. Park, H. et al. Observation of fractionally quantized anomalous Hall effect. *Nature* **622**, 74–79 (2023).
4. Xu, F. et al. Observation of integer and fractional quantum anomalous Hall effects in twisted bilayer $MoTe_2$. *Phys. Rev. X* **13**, 031037 (2023).
5. Cai, J. et al. Signatures of fractional quantum anomalous Hall states in twisted $MoTe_2$. *Nature* **622**, 63–68 (2023).
6. Zeng, Y. et al. Thermodynamic evidence of fractional Chern insulator in moiré $MoTe_2$. *Nature* **622**, 69–73 (2023).
7. Uri, A. et al. Mapping the twist-angle disorder and Landau levels in magic-angle graphene. *Nature* **581**, 47–52 (2020).
8. Spanton, E. M. et al. Observation of fractional Chern insulators in a van der Waals heterostructure. *Science* **360**, 62–66 (2018).
9. Cao, Y. et al. Correlated insulator behaviour at half-filling in magic-angle graphene superlattices. *Nature* **556**, 80–84 (2018).
10. Chen, G. et al. Evidence of a gate-tunable Mott insulator in a trilayer graphene moiré superlattice. *Nat. Phys.* **15**, 237–241 (2019).
11. Regan, E. C. et al. Mott and generalized Wigner crystal states in WSe_2/WS_2 moiré superlattices. *Nature* **579**, 359–363 (2020).
12. Tang, Y. et al. Simulation of Hubbard model physics in WSe_2/WS_2 moiré superlattices. *Nature* **579**, 353–358 (2020).
13. Wang, L. et al. Correlated electronic phases in twisted bilayer transition metal dichalcogenides. *Nat. Mater.* **19**, 861–866 (2020).
14. Shimazaki, Y. et al. Strongly correlated electrons and hybrid excitons in a moiré heterostructure. *Nature* **580**, 472–477 (2020).
15. Xu, Y. et al. Correlated insulating states at fractional fillings of moiré superlattices. *Nature* **587**, 214–218 (2020).
16. Sharpe, A. L. et al. Emergent ferromagnetism near three-quarters filling in twisted bilayer graphene. *Science* **365**, 605–608 (2019).
17. Serlin, M. et al. Intrinsic quantized anomalous Hall effect in a moiré heterostructure. *Science* **367**, 900–903 (2020).
18. Chen, G. et al. Tunable correlated Chern insulator and ferromagnetism in a moiré superlattice. *Nature* **579**, 56–61 (2020).
19. Li, T. et al. Quantum anomalous Hall effect from intertwined moiré bands. *Nature* **600**, 641–646 (2021).
20. Anderson, E. et al. Programming correlated magnetic states with gate-controlled moiré geometry. *Science* **381**, 325–330 (2023).
21. Xie, Y. et al. Fractional Chern insulators in magic-angle twisted bilayer graphene. *Nature* **600**, 439–443 (2021).
22. Ji, Z. et al. Local probe of bulk and edge states in a fractional Chern insulator. Preprint at https://arxiv.org/abs/2404.07157 (2024).
23. Lu, Z. et al. Fractional quantum anomalous Hall effect in multilayer graphene. *Nature* **626**, 759–764 (2024).
24. Li, H., Kumar, U., Sun, K. & Lin, S.-Z. Spontaneous fractional Chern insulators in transition metal dichalcogenide moiré superlattices. *Phys. Rev. Res.* **3**, L032070 (2021).
25. Dong, Z., Patri, A. S. & Senthil, T. Theory of quantum anomalous Hall phases in pentalayer rhombohedral graphene moiré structures. Preprint at https://arxiv.org/abs/2311.03445 (2023).
26. Dong, Z., Patri, A. S. & Senthil, T. Stability of anomalous Hall crystals in multilayer rhombohedral graphene. Preprint at https://arxiv.org/abs/2403.07873 (2024).
27. Wang, C. et al. Fractional Chern insulator in twisted bilayer $MoTe_2$. *Phys. Rev. Lett.* **132**, 036501 (2024).
28. Yu, J. et al. Fractional Chern insulators versus nonmagnetic states in twisted bilayer $MoTe_2$. *Phys. Rev. B* **109**, 045147 (2024).
29. Morales-Durán, N., Wei, N., Shi, J. & MacDonald, A. H. Magic angles and fractional Chern insulators in twisted homobilayer transition metal dichalcogenides. *Phys. Rev. Lett.* **132**, 096602 (2024).
30. Jia, Y. et al. Moire fractional Chern insulators. I. First-principles calculations and continuum models of twisted bilayer $MoTe_2$. *Phys. Rev. B* **109**, 205121 (2024).
31. Sheng, D. N., Reddy, A. P., Abouelkomsan, A., Bergholtz, E. J. & Fu, L. Quantum anomalous Hall crystal at fractional filling of moiré superlattices. *Phys. Rev. Lett.* **133**, 066601 (2024).
32. Dong, J. et al. Anomalous Hall crystals in rhombohedral multilayer graphene. I. Interaction-driven Chern bands and fractional quantum Hall states at zero magnetic field. Preprint at https://arxiv.org/abs/2311.05568 (2023).
33. Soejima, T. et al. Anomalous Hall crystals in rhombohedral multilayer graphene. II. General mechanism and a minimal model. Preprint at https://arxiv.org/abs/2403.05522 (2024).
34. Goldman, H., Reddy, A. P., Paul, N. & Fu, L. Zero-field composite Fermi liquid in twisted semiconductor bilayers. *Phys. Rev. Lett.* **131**, 136501 (2023).
35. Anahory, Y. et al. SQUID-on-tip with single-electron spin sensitivity for high-field and ultra-low temperature nanomagnetic imaging. *Nanoscale* **12**, 3174–3182 (2020).
36. Dong, J., Wang, J., Ledwith, P. J., Vishwanath, A. & Parker, D. E. Composite Fermi liquid at zero magnetic field in twisted $MoTe_2$. *Phys. Rev. Lett.* **131**, 136502 (2023).
37. Jain, J. K. Composite-fermion approach for the fractional quantum Hall effect. *Phys. Rev. Lett.* **63**, 199–202 (1989).
38. Deilmann, T., Krüger, P. & Rohlfing, M. *Ab initio* studies of exciton *g* factors: monolayer transition metal dichalcogenides in magnetic fields. *Phys. Rev. Lett.* **124**, 226402 (2020).
39. Woźniak, T., Faria Junior, P. E., Seifert, G., Chaves, A. & Kunstmann, J. Exciton *g* factors of van der Waals heterostructures from first-principles calculations. *Phys. Rev. B* **101**, 235408 (2020).
40. Robert, C. et al. Measurement of conduction and valence bands *g*-factors in a transition metal dichalcogenide monolayer. *Phys. Rev. Lett.* **126**, 067403 (2021).
41. Morf, R. & Halperin, B. I. Monte Carlo evaluation of trial wave functions for the fractional quantized Hall effect: disk geometry. *Phys. Rev. B* **33**, 2221–2246 (1986).
42. Yang, F. et al. Experimental determination of the energy per particle in partially filled Landau levels. *Phys. Rev. Lett.* **126**, 156802 (2021).
43. Grover, S. et al. Chern mosaic and Berry-curvature magnetism in magic-angle graphene. *Nat. Phys.* **18**, 885–892 (2022).
44. Nakamura, J., Liang, S., Gardner, G. C. & Manfra, M. J. Direct observation of anyonic braiding statistics. *Nat. Phys.* **16**, 931–936 (2020).

Methods

Device fabrication

Devices used in this study are fabricated using methods previously described in the literature. Transport data from device A was previously reported in ref. 3, in which it appears as device D (3.7°). Device B was previously studied in ref. 5.

nSOT sensor fabrication and local magnetometry measurements

We perform magnetic imaging with a superconducting quantum interference device on the apex of a sharp quartz pipette (nSOT)[1,2,35]. We use a quartz micropipette with an inner tube diameter of 0.5 mm to pull a sharp tip with an apex diameter of about 150 nm. To form the coarse contacts, we deposit gold films by electron beam evaporation at a deposition rate of 2 Å s^{-1} to produce a thickness of (50 Å Ti/500 Å Au). A shunt resistor is further deposited with (80 Å Ti/150 Å Au) within 500 μm from the tip apex, resulting in an approximately 10 Ω shunt resistance. We next cover the coarse contact pads with a thick layer of indium solder to minimize contact resistance and to improve contact with the leaf springs used to hold the tip in the holder. We then evaporate indium in a custom-built thermal evaporator at three angles to cover two contacts at 110° to the apex, with a head-on deposition performed last. The tip holder is mounted on a cryostat and protected by radiation shielding and LN_2 jacketing. It is kept at a temperature of 20 K throughout the deposition process. Each evaporation step is preceded by 5–10 min of thermalization time during which the evaporator chamber is flooded with He exchange gas at a pressure of 5×10^{-3} mbar. Typical thicknesses for the indium depositions are 350 Å for the side contacts and 300 Å for the head-on deposition for 150 nm tip diameter, with a 1 Å s^{-1} deposition rate for all steps. These parameters enable a highly uniform, low-grain-size film to form near the tip apex (Extended Data Fig. 1a).

The magnetic field at the tip apex is read out by measuring the tip in a quasi-voltage bias configuration using a series SQUID array amplifier (SSAA)[45]. To calibrate the sensitivity of the nSOT, we measure the frequency domain output of the SSAA amplifiers at the nSOT operating point. The nSOT voltage is converted to magnetic field by the transfer function, which we measure by monitoring the d.c. output voltage response to about 20 μT step in the magnetic field. This gives the transfer function in units of V T^{-1}. As shown in Extended Data Fig. 1b, our nSOT sensors show a maximum sensitivity (typically near a flux bias point of $\Phi_0/2$) of about 300 pT $Hz^{-1/2}$ with an effective diameter of 200 nm, corresponding to about $6n\Phi_0$ $Hz^{-1/2}$.

Magnetization reconstruction

To reconstruct the magnetization, we follow standard Fourier domain techniques (see, for example, the supplementary information of ref. 46). The magnetization shown in the main text is computed by performing zero padding of the measured magnetic field map before Fourier transforms are computed. This constitutes an unphysical assumption about magnetic fields outside the measurement area that were not constrained experimentally—that is, that they vanish—and constitutes a source of systematic error.

To address this source of error in m, we analyse the influence of the choice of padding on the reconstructed magnetization (Extended Data Fig. 9). Our base model assumes zero magnetic field outside the region in which the fields are measured. We then compare this to two alternative assumptions: first, we replicate the signal between the contacts on the left and right sides of the frame, extending the finite magnetic fields observed at the boundary into a region 500 nm wide. As a second comparative model, we extend the fields on the edge of this region by an additional 500 nm above and below the measured region. As shown in Extended Data Fig. 9, the reconstructed magnetization differs from the base model by about 10% in the neighbourhood of both $\nu = -1$ and $-2/3$, with comparable or smaller effects on the inferred gap size.

Magnetization reconstruction error analysis

Although some uncertainty is contributed by the calibration of our magnetometer (which we measure to a reproducibility of approximately 5%), systematic errors are probably more substantial. One source of error arises from the fact that our measurement window does not capture the entire region of the physical magnetic field. Because magnetic dipole fields are long-range, the magnetic inversion algorithm takes as an input both the field in the measured region and an assumed field outside the measured region. In the data shown in the main text, this field is assumed to be zero. To estimate the magnitude of the error resulting from this assumption, we compare m calculated using zero padding to calculations done with different physically motivated padding assumptions (Methods and Extended Data Fig. 9). Across several models, we find that m is consistent to within 10%. A second source of uncertainty is conceptual and arises from our empirical definition of the thermodynamic gap, for which we assume that the region of the steepest negative slope in m arises entirely from the chiral edge states. Although this is known to be true in the clean limit for fractional Hall states in partially filled Landau levels, theoretical calculations accounting for the effects of finite disorder and inhomogeneous Berry curvature are not available to justify this empirical definition of the thermodynamic energy gap.

Measurement conditions for presented data

All voltages indicated denote root mean square values. The external magnetic field was kept constant at 34 mT.

Figure 1a and Extended Data Figs. 2e and 6: transfer function = 100 V T^{-1}; height = 150 nm; δv_s = 20 mV; $\delta n = 2.7 \times 10^{10}$ cm^{-2}; δD = 0.5 mV nm^{-1}; frequency = 511.777 Hz.

Figure 1b,c and Extended Data Figs. 2d, 4 and 5: transfer function = 250 V T^{-1}; height = 100 nm; δv_t = 40.1 mV; δv_b = 35.8 mV; $\delta n = 3.8 \times 10^{10}$ cm^{-2}; frequency = 151.777 Hz.

Figure 1d,e: transfer function = 500 V T^{-1}; height = 50 nm; δv_t = 4.1 mV; δv_b = 3.6 mV; $\delta n = 3.8 \times 10^{9}$ cm^{-2}; frequency = 511.777 Hz.

Figure 1f: transfer function = 500 V T^{-1}; height = 50 nm; δv_t = 40.1 mV; δv_b = 35.8 mV; $\delta n = 3 \times 10^{10}$ cm^{-2}; frequency = 90.777 Hz.

Figure 1f (inset): transfer function = 500 V T^{-1}; height = 50 nm; δv_t = 20 mV; δv_b = 18 mV; $\delta n = 1.9 \times 10^{10}$ cm^{-2}; frequency = 90.777 Hz.

Figures 2 and 4a–c,e: transfer function = 280 V T^{-1}; height = 190 nm; δv_b = 40 mV; $\delta n = 2.1 \times 10^{10}$ cm^{-2}; δD = 2 mV nm^{-1}; frequency = 511.777 Hz.

Figure 3a: transfer function = 500 V T^{-1}; height = 100 nm; δv_s = 5 mV; $\delta n = 5 \times 10^{9}$ cm^{-2}; frequency = 151.777 Hz.

Figure 3b: transfer function = 500 V T^{-1}; height = 100 nm; δv_s = 20 mV; $\delta n = 2.1 \times 10^{10}$ cm^{-2}; δD = 2 mV nm^{-1}; frequency = 151.777 Hz.

Figure 4d: transfer function = 500 V T^{-1}; height = 50 nm; δv_t = 60.6 mV; δv_b = −53 mV; δD = 5 mV nm^{-1}; frequency = 1151.777 Hz.

Figure 4f: transfer function = 500 V T^{-1}; height = 190 nm; δv_s = 50 mV; $\delta n = 5 \times 10^{10}$ cm^{-2}; frequency = 511.777 Hz.

Extended Data Fig. 2f: transfer function = 100 V T^{-1}; height = 180 nm; δv_s = 28 mV; $\delta n = 4.2 \times 10^{10}$ cm^{-2}; frequency = 251.777 Hz.

Extended Data Fig. 3: transfer function = 500 V T^{-1}; height = 100 nm; δv_b = 28 mV; $\delta n = 4.2 \times 10^{10}$ cm^{-2}; frequency = 251.777 Hz.

Data availability

All data are available at Dryad (https://doi.org/10.5061/dryad.0zpc86769) (ref. 47).

Code availability

All the software supporting the data processing pipeline is available at Zenodo (https://doi.org/10.5281/zenodo.13621665) (ref. 48).

45. Huber, M. E. et al. DC SQUID series array amplifiers with 120 MHz bandwidth. *IEEE Trans. Appl. Supercond.* **11**, 1251–1256 (2001).

46. Tschirhart, C. L. et al. Imaging orbital ferromagnetism in a moiré Chern insulator. *Science* **372**, 1323–1327 (2021).
47. Redekop, E. et al. Direct magnetic imaging of fractional Chern insulators in twisted $MoTe_2$. *Dryad* https://doi.org/10.5061/dryad.0zpc86769 (2024).
48. Redekop, E. et al. Direct magnetic imaging of fractional Chern insulators in twisted $MoTe_2$. *Zenodo* https://doi.org/10.5281/zenodo.13621665 (2024).

Acknowledgements We thank L. Fu, T. Wang and M. Zaletel for the discussions. Work at UCSB was primarily supported by the Army Research Office under award no. W911NF-20-2-0166. E.R. and O.S. acknowledge support by the National Science Foundation through Enabling Quantum Leap: Convergent Accelerated Discovery Foundries for Quantum Materials Science, Engineering and Information (Q-AMASE-i) award no. DMR-1906325. A.F.Y. acknowledges additional support from the Gordon and Betty Moore Foundation EPIQS programme under award no. GBMF9471. A.F.Y. also acknowledges the support of the W. M. Keck Foundation under award no. SB190132 for the development of SQUID microscopy techniques. Work at the University of Washington was supported by DoE BES under award no. DE-SC0018171. Device fabrication used the facilities and instrumentation supported by NSF MRSEC DMR-230879. K.W. and T.T. acknowledge support from the Elemental Strategy Initiative conducted by the MEXT, Japan (grant no. JPMXP0112101001) and JSPS KAKENHI (grant nos. 19H05790, 20H00354 and 21H05233).

Author contributions E.R., A.F.Y. and X.X. initiated the experiment. H.P., J.C. and E.A. prepared the samples. K.W. and T.T. grew the hBN crystals. E.R. and C.Z. performed the measurements and data analysis. O.S., T.A., G.B. and S.S. prepared the nanoSQUID-on-tip. E.R., T.A. and O.S. developed the nanoSQUID microscope. M.E.H. provided Series SQUID Array Amplifiers for the nSOT readout. E.R. and A.F.Y. wrote the paper with input from all other authors.

Competing interests The authors declare no competing interests.

Additional information

Supplementary information The online version contains supplementary material available at https://doi.org/10.1038/s41586-024-08153-x.

Correspondence and requests for materials should be addressed to Andrea F. Young.

Peer review information *Nature* thanks Yonglong Xie and the other, anonymous, reviewer(s) for their contribution to the peer review of this work. Peer reviewer reports are available.

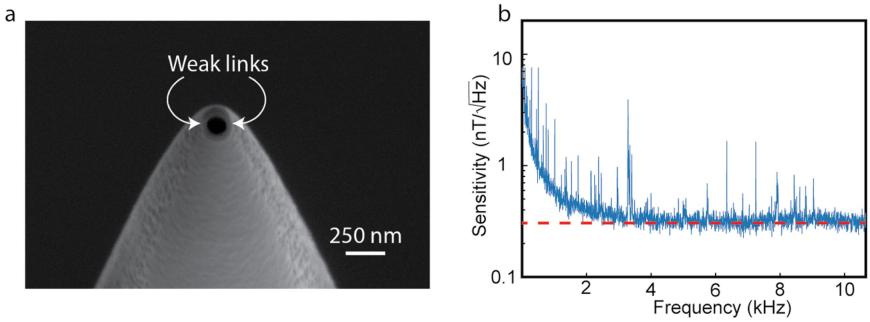

Extended Data Fig. 1 | SQUID sensitivity. (**a**) SEM image of the nSOT sensor used in most of the current work, highlighting the superconducting weak links on the tip apex. (**b**) Typical sensitivity of the nSOT as a function of the frequency. $1/f$ noise dominates at frequencies below 1 kHz and decays below the instrumentation noise floor above 2 kHz allowing for ultra-high magnetic field sensitivity well below 1nT/$\sqrt{\text{Hz}}$.

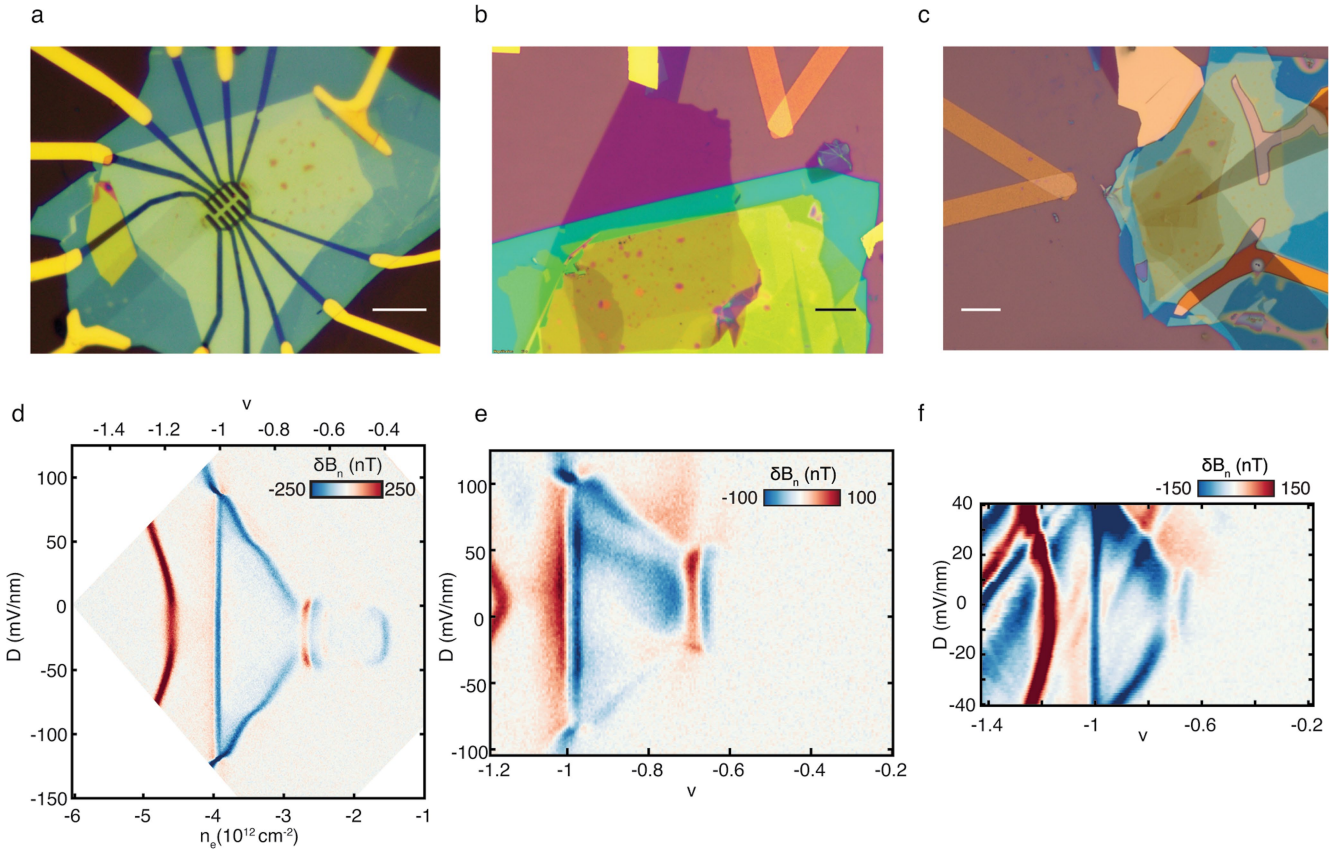

Extended Data Fig. 2 | Devices. (**a**) Optical micrograph of Device A (corresponding to device D(3.7°) from ref. 3); (**b**) Device B (corresponding to device from ref. 5); (**c**) Device C. Scale bar is 10 μm; (**d**) δB_n phase diagram measured in Device A, (**e**) Device B, and (**f**) device C. All devices show signals near $\nu = -1$ and $\nu = -2/3$ characteristic of Chern insulators.

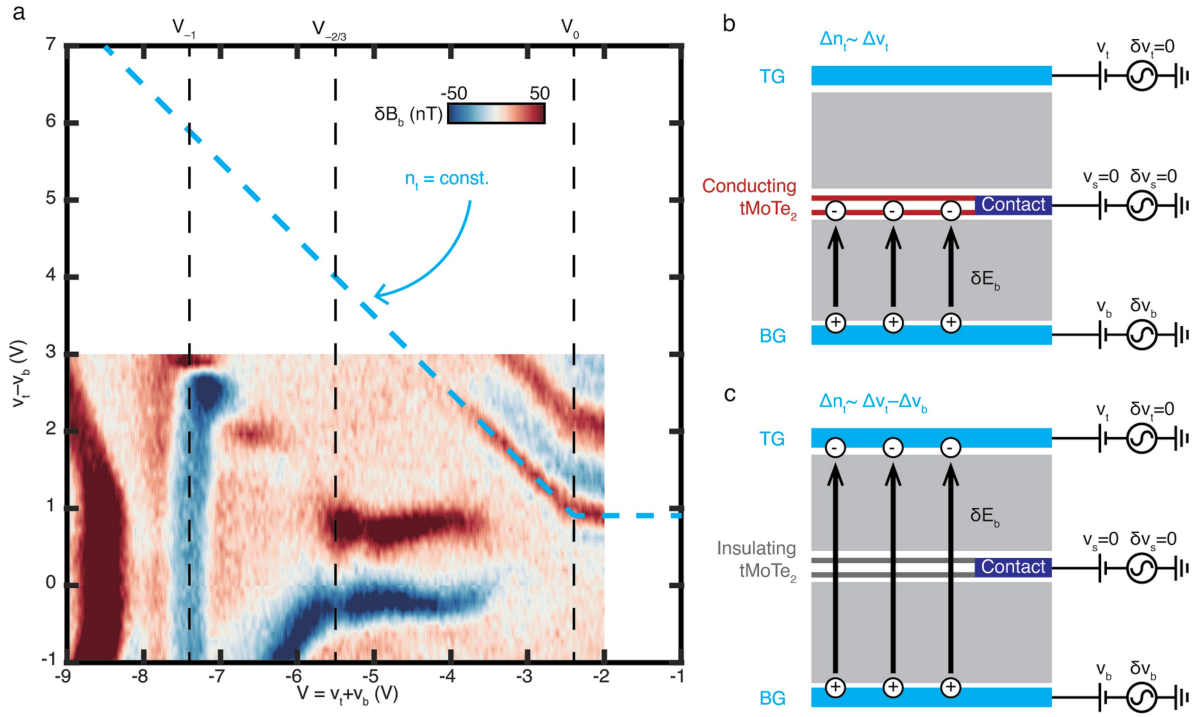

Extended Data Fig. 3 | Chemical potential sensing and band edge offset. (**a**) δB_b for device C as a function of $V \equiv v_t + v_b$ and $v_t - v_b$ in the configuration with the sample grounded. The phase diagram exhibits both $MoTe_2$ features described in the main text as well as features associated with Landau levels of the top graphite gate. The band edge is visible as a kink in the constant top gate carrier density trajectory, marked as a dashed blue line, with the offset V_0 corresponding to the voltage that separates the regime where $tMoTe_2$ is insulating and the regime where it is hole-doped. The value obtained using this method agrees with that described in the main text using the $\nu = -1$ and $\nu = -2/3$ gap densities. (**b**) Schematic of the electric field in the hole-doped $tMoTe_2$ regime. Here modulations of the bottom gate produce electric fields δE_b which are screened by the $tMoTe_2$ layer. In this regime, the top gate density n_t is tuned solely by V_t, and trajectories of constant n_t follow slope −1 on the diagram in panel **a**. (**c**) Schematic of the electric field in the insulating $tMoTe_2$ regime. Here δE_b penetrates the $tMoTe_2$, so that n_t is tuned by both v_t and v_b. In this regime, constant-n_t lines have slope 0 in panel **a**.

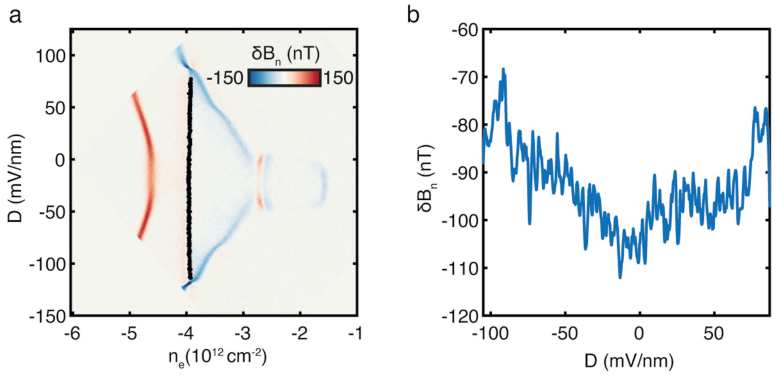

Extended Data Fig. 4 | Chern insulator signal dependence on the displacement field. (**a**) Signal δB_n as a function of charge carrier density and electric displacement field; (**b**) Minimum value of δB_n in a window around $\nu = -1$ gap along displacement field axis. The positions of the values are shown on **a**. The signal from the gap decays slightly as a function of displacement field, remaining finite up to the first order phase transition induced by layer polarization.

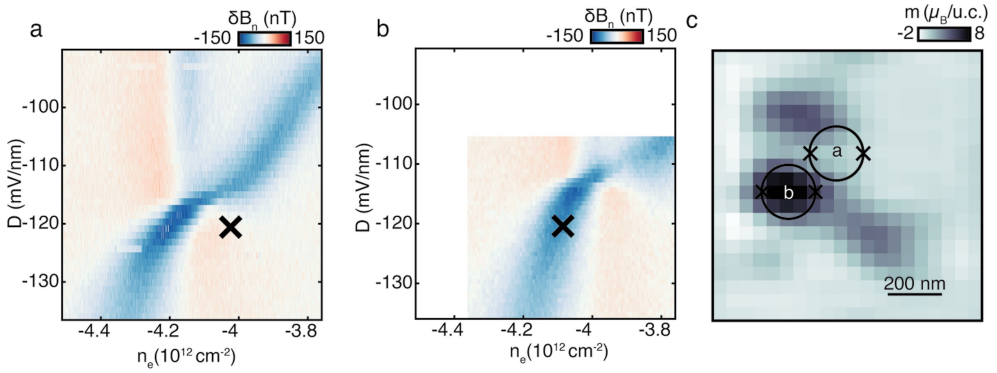

Extended Data Fig. 5 | First order valley polarization transition at $\nu = -1$. (**a**) δB_n near the valley polarization transition in the vicinity of $\nu = -1$ at point "a" in panel c. (**b**) δB_n measured at point "b", approximately 200 nm away from point "a". Both panel a and b show a sharp first-order-like signal on the boundary of the $\nu = -1$ Chern insulator peak, but these transitions appear at slightly different values of D and n_e. (**c**) Reconstructed magnetization in the point indicated by the "×" on panels a and b. The measured m at position "a" is consistent with zero to within our experimental error, and we find no evidence for non-zero net magnetization in the high $|D|$ phases. The non-zero signal observed in δB_n at that position is associated with fringe AC magnetic fields arising from areas where where the "×" position in parameter space corresponds to the valley transition.

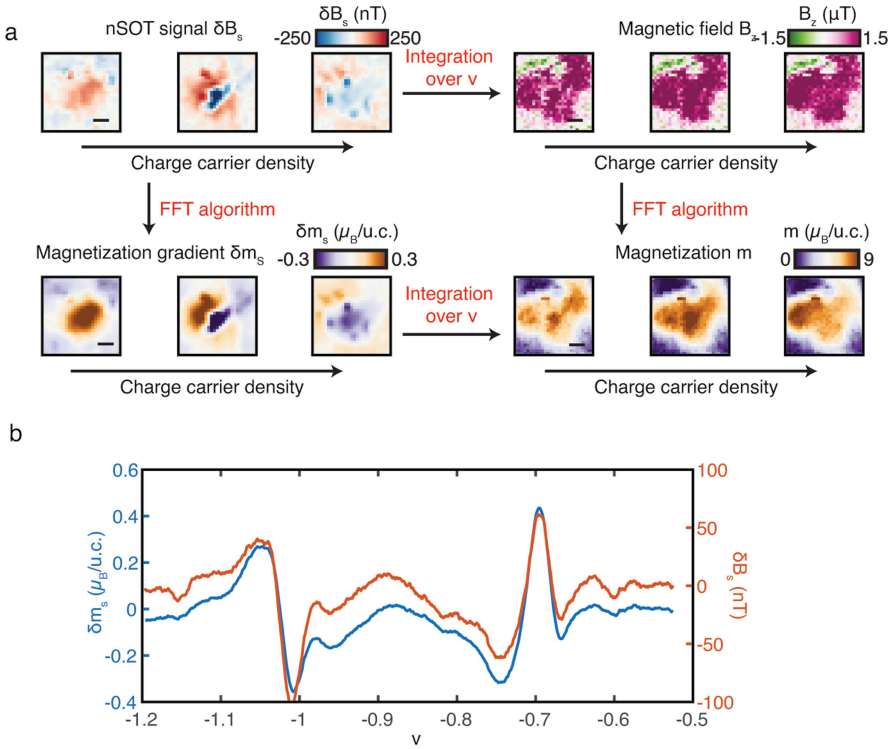

Extended Data Fig. 6 | Magnetization reconstruction. (**a**) Schematic of analysis to reconstruct the magnetization. We measure the local magnetic field δB_s in response to a modulated sample voltage δv_s; data is from Device B, with scale bar of 2 μm. An FFT-based algorithm (see Methods) can be used to directly compute the corresponding δm_s, which may then be integrated over v_s to obtain m. Alternatively, the δB_s signal may be integrated over V_s to obtain B, which can in some cases be compared to the directly measured B_{DC}; this can them be processed by the FFT algorithm to produce the same m. (**b**) Comparison of the measured δB_s (orange) and the reconstructed δm_s (blue) as a function of the filling factor v at a single given spatial location. While qualitative features are preserved, but of course quantitative features differ.

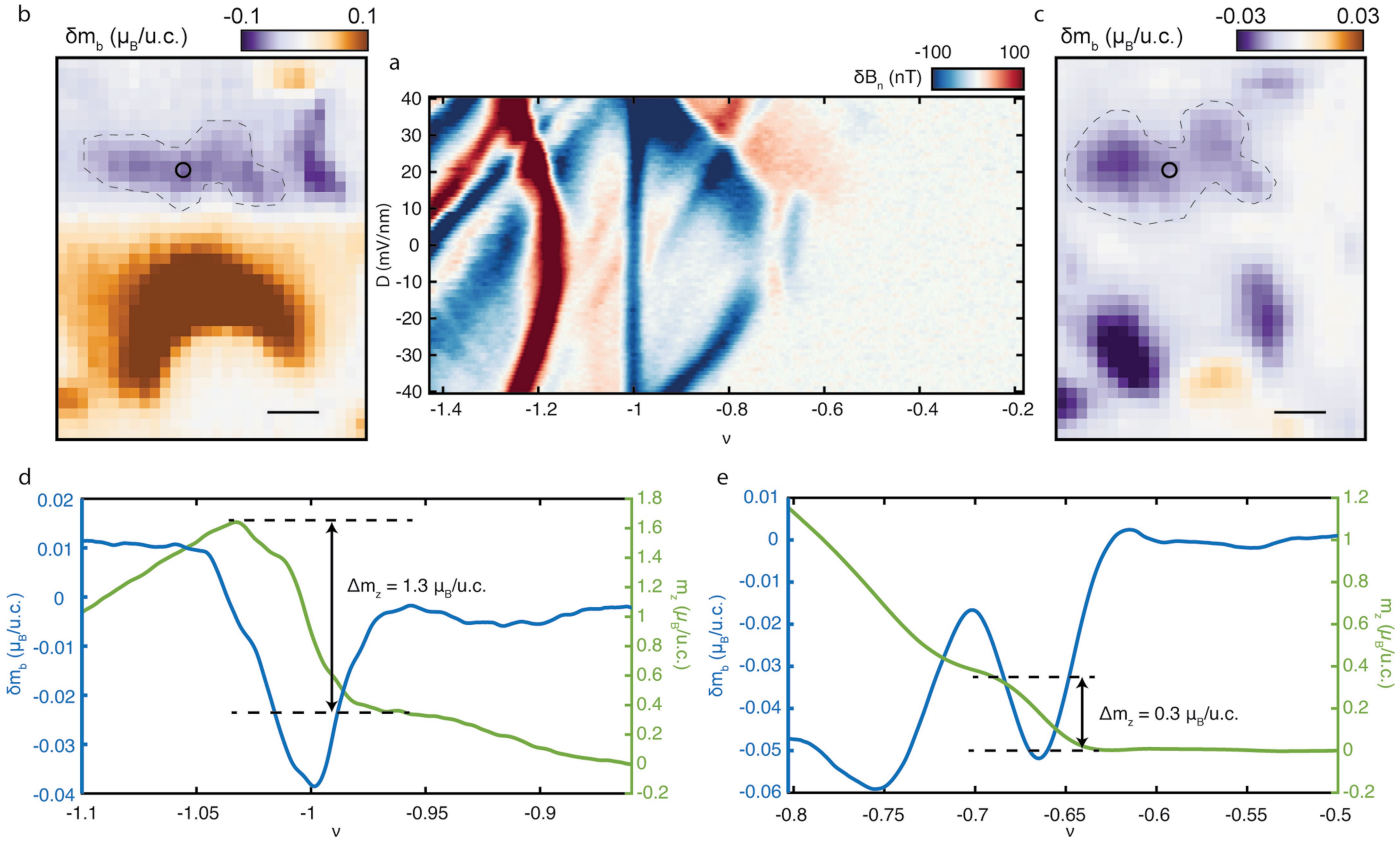

Extended Data Fig. 7 | Gap reconstruction in device C. (**a**) δB_n with an applied modulation of $\delta n \approx 1.5 \times 10^{10}$ cm^{-2}; (**b**) Spatial distribution of δm_b in the vicinity of $\nu = -1$ gap. The dashed line outlines the region of the device in the $\nu = -1$ gap. Scale bar is 500 nm; (**c**) Spatial distribution of δm_b in the vicinity of $\nu = -2/3$ gap. The dashed line outlines the region of the device in the $\nu = -2/3$ gap; (**d**) Reconstructed magnetization drop of $\Delta m = 1.3 \mu_B/u.c.$ corresponding to the thermodynamic gap $^{-1}\Delta = 13$ meV across the $\nu = -1$ gap in the point circled on **b**; (**e**) Reconstructed magnetization drop of $\Delta m = 0.3 \mu_B/u.c.$ corresponding to the thermodynamic gap $^{-2/3}\Delta = 5$ meV across the $\nu = -2/3$ gap in the point circled on **c**.

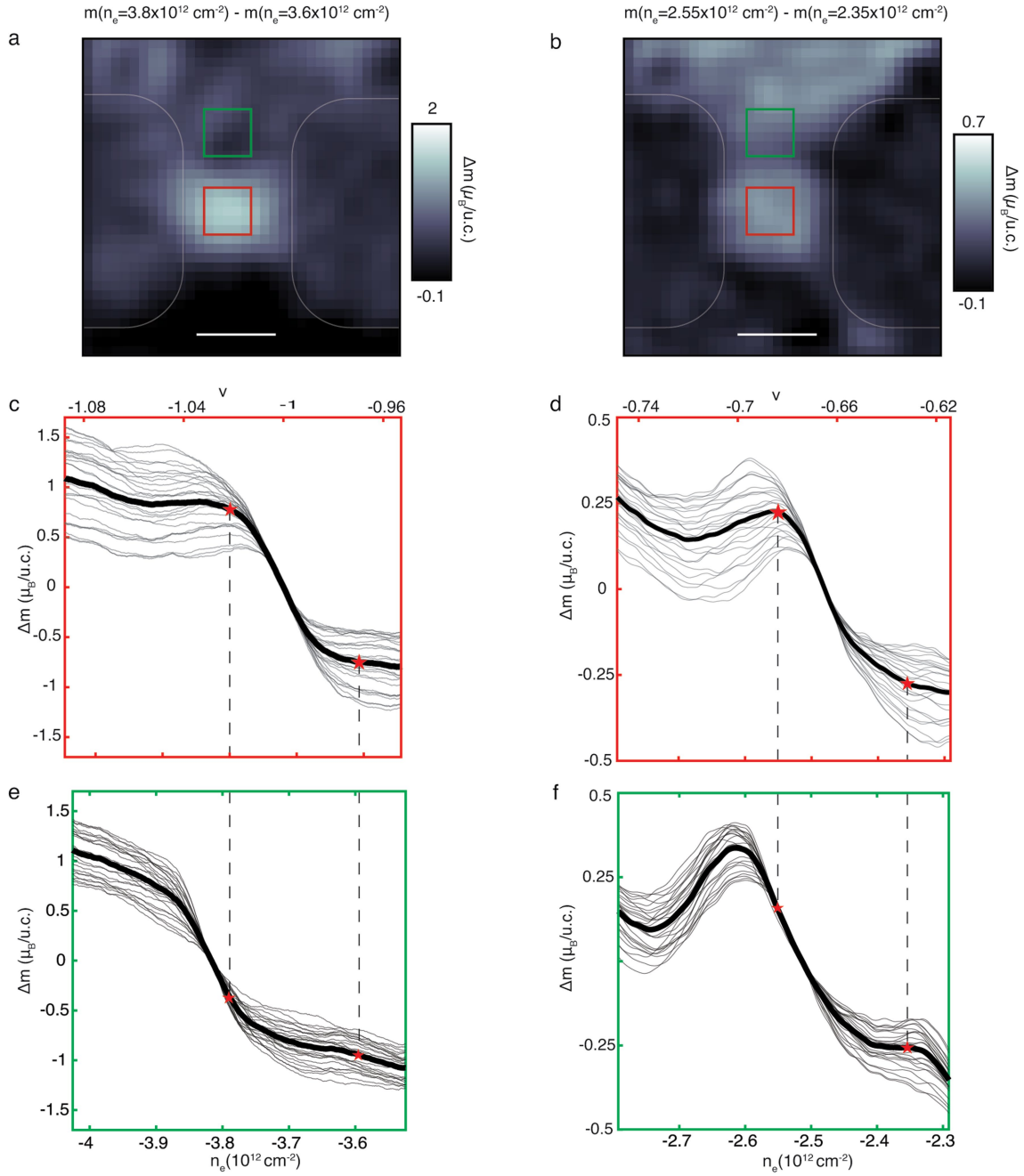

Extended Data Fig. 8 | Magnetization near $\nu = -1$ and $\nu = -2/3$. (**a**) Spatial image corresponding to $\Delta m = m(n_e = 3.8 \times 10^{12}\,\mathrm{cm}^{-2}) - m(n_e = 3.6 \times 10^{12}\,\mathrm{cm}^{-2})$ near filling $\nu = -1$. Scale bar is 500 nm; (**b**) Spatial image corresponding to $m(n_e = 2.55 \times 10^{12}\,\mathrm{cm}^{-2}) - m(n_e = 2.35 \times 10^{12}\,\mathrm{cm}^{-2})$, near filling $\nu = -2/3$ in the same region as panel **a**. Scale bar is 500 nm; (**c**) $\Delta m(n_e)$ (referenced to the center of the local $\nu = -1$ gap) measured at 25 points within the red square in panel **a**. The black curve is the average. Red stars indicate the charge carrier densities used to determine spatial distribution of Δm in panel **a**; (**d**) $\Delta m(n_e)$ (referenced to the center of the local $\nu = -2/3$ gap) measured at 25 points within the red square in panel **b**. The black curve is the average. Red stars indicate the charge carrier densities used to determine spatial distribution of Δm in panel **b**; (**e**) $\Delta m(n_e)$ (referenced to the center of the local $\nu = -1$ gap) measured at 25 points within the green square in panel **a**. The black curve is the average. Red stars indicate the charge carrier densities used to determine spatial distribution of Δm in panel **a**; (**f**) $\Delta m(n_e)$ (referenced to the center of the local $\nu = -2/3$ gap) measured at 25 points within the green square in panel **b**. The black curve is the average. Red stars indicate the charge carrier densities used to determine spatial distribution of Δm in panel **b**.

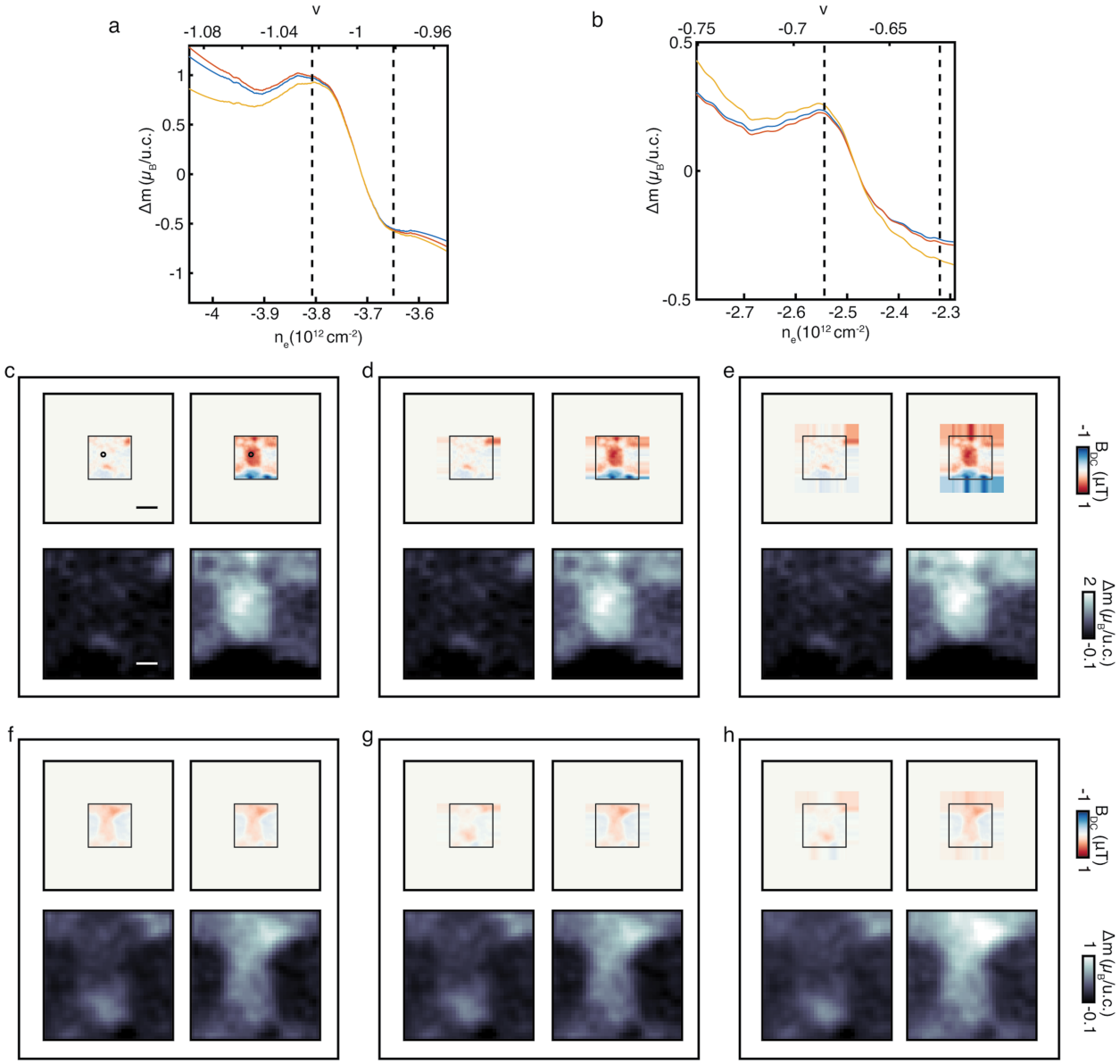

Extended Data Fig. 9 | Estimating systematic error due to padding assumptions. (**a**) Magnetization change Δm (referenced to the center of the $\nu = -1$ gap) in the same location as that shown in Fig. 3 for the three different padding assumptions described in panels c, d, and e. (**b**) Magnetization change Δm (referenced to the center of the $\nu = -2/3$ gap) in the same location as that shown in Fig. 3 for the three different padding assumptions described in panels f, g, and h. (**c**) Top row: measured B_{DC} with zero padding assumption across the $\nu = -1$ gap. Scale bar is 600 nm. Left and right panels correspond to n_e values shown by dotted lines in panel a. Bottom row: reconstructed magnetization in the measured range at the same positions, with the zero padding assumption. The magnetization change across the gap is 1.61 μ_B/u.c. Scale bar is 200 nm. (**d**) Same as panel c, except with the padding assumption that data extends to the right and left of measured area as shown. The magnetization change across the gap is 1.66 μ_B/u.c. (**e**)Same as panels c and d but with additional padding as shown. Magnetization change across the gap is 1.57 μ_B/u.c. (**f**) Top row: measured B_{DC} with zero padding assumption across the $\nu = -2/3$ gap. Left and right panels correspond to n_e values shown by dotted lines in panel **b**. Bottom row: reconstructed magnetization in the measured range at the same positions, with the zero padding assumption. The magnetization change across the gap is 0.52 μ_B/u.c. (**g**) Same as panel f, with the same padding assumption as panel **d**. Magnetization change across the gap is 0.52 μ_B/u.c.; (**h**) Same as panels f-g but with the same padding assumption as in panel **e**. Magnetization change across the gap is 0.58 μ_B/u.c.